MECHANICS OF THE PUSH-OUT PROCESS FROM *IN SITU* MEASUREMENT OF THE STRESS DISTRIBUTION ALONG EMBEDDED SAPPHIRE FIBERS

QING MA[1], LEI CAROL LIANG[2], D. R. CLARKE[1] and J. W. HUTCHINSON[2]

[1]Materials Department, University of California, Santa Barbara, CA 93106 and [2]Division of Applied
Sciences, Harvard University, Cambridge, MA 02138, U.S.A.

Abstract—The basic mechanics of the fiber push-out process are studied by measuring the stress distributions along *c*-axis sapphire fibers in γ-TiAl matrices. The stress measurements were made *in situ* during fiber push-out tests using a piezo-spectroscopy method. By focussing an optical microprobe into a sapphire fiber, the frequency shift distribution of the characteristics R lines of Cr^{3+}, and hence the stress distribution along the fiber were determined at each increment of applied load. By comparing the measured stress distributions with ones calculated using finite element method, key mechanical parameters including residual stress before composite slicing, debond length at each load, debond energy and the frictional stress along the interface in both debonding and sliding phases were determined. Two coating systems (Mo/Al_2O_3 and $CVD-C/Al_2O_3$) were studied. The results also show that while the debond energies differ by an order of magnitude, the frictional stresses are very similar in magnitude, suggesting that the interface morphology is of greater importance than the nature of the coating.

1. INTRODUCTION

The fiber push-out test [1, 2] has become an invaluable method of evaluating the mechanical response of fibers in a matrix. Its attraction stems from both its relative simplicity as a test method and from the fact that actual embedded fibers in a composite can be probed. One draw back however is that very little data about each fiber is actually obtained from the test. Normally the push-out load is recorded as a function of fiber displacement. From this only the average effective frictional stress along the debonded interface can be obtained with reasonable accuracy during the fiber sliding process (the sliding phase) after the whole interface debonds, and when large displacement occurs. Attempts to deduce information about the interface debonding process (the debonding phase), prior to the sliding phase, from the load–displacement curve have been made. For example, the load drop at the transition between the debonding phase and the sliding phase has been used to estimate the interface debond energy Γ. Unfortunately, any connection between the load drop and Γ is obscured by two problems. First, the steady state debonding process necessarily assumed in deriving any relationship between load drop and Γ has not been confirmed rigorously by experiments. In fact, recent calculations [3] indicate that the debonding can be unstable, at least under certain conditions. Secondly, it has been demonstrated that due to the asperity roughness of the interface, there is an "unseating" effect at the transition, which may increase the apparent load

drop [4]. Any such surface morphology also affects the interpretation of the frictional resistance, τ, obtained during the sliding phase, where large sliding distances averaging the asperity effect along the fiber occurs. The measured frictional resistance may therefore not be relevant for the debonding and sliding process experienced in brittle matrix composites where only a small amount of sliding may occur before the fiber fractures.

In this contribution, we show that considerably more data is obtainable from the push-out test when the stress distribution along the fibers *during* the push-out process is determined. Such stress distribution measurements were made using techniques similar to that used in an earlier work [5], where residual stresses in embedded fibers were measured. This measurement technique is based on the piezo-spectroscopic properties of Cr^{+3} ions in sapphire, in which the characteristic fluorescence R lines shift linearly with hydrostatic stress components. For the axisymmetric problems of a *c*-axis fiber embedded perpendicular to the composite surface, the shift Δv depend on the radial stress σ_r and axial stress σ_z according to the following relationship

$$\Delta v = 2\Pi_a \sigma_r + \Pi_c \sigma_z \qquad (1)$$

where Π_a and Π_c are the piezo-spectroscopic coefficients for the a and c directions. They have been measured to have value of 2.70 and 2.15 $cm^{-1} GPa^{-1}$, respectively [6]. A positive shift implies tension and a negative shift implies compression. The frequency
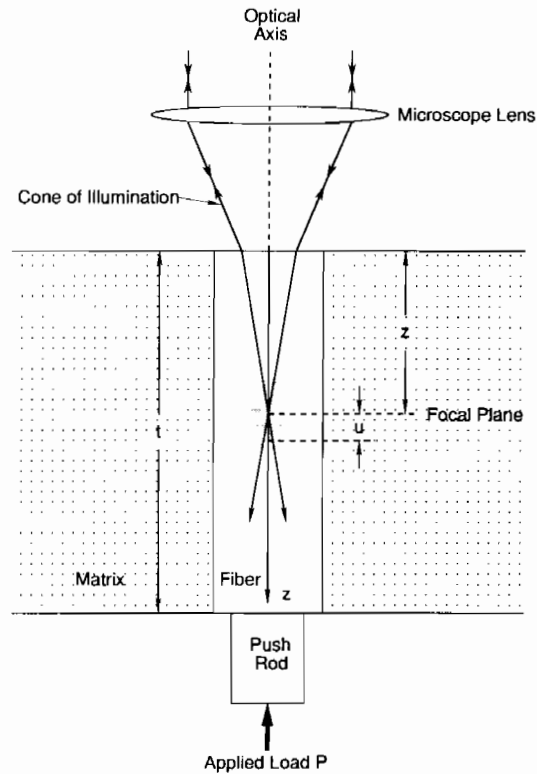
Fig. 1. Schematic diagram of the optical arrangement used to collect fluorescence from a region in an embedded sapphire fiber under push-out load. When the laser excitation is focused at a distance z below the top surface, only the signal generated in a small volume above and below the focal plane is effectively collected by the lens.

measurements were implemented using an optical microscope having a small depth of field to both excite and collect the fluorescence signals around its focal point. The depth profile of the frequency shift is measured as a function of depth z through an exposed fiber end as the point of focus was moved successively deeper. The detailed methodology will be described in Section 2.

In our experiments, a load is applied at one end of the fiber, and is increased in several discrete steps until total interface debond occurs. At each load, the fluorescence shift distribution along the entire sapphire fiber is measured through the other end of the fiber. Several fibers with two different coatings (molybdenum and CVD-graphite) were measured whilst under load in the pushed-out test. In preliminary experiments, it was observed that the fibers with the same coating behave in a similar manner. In Section 3, the measured shift distributions in both debonding phase and sliding phase will be presented for two fibers with the two different coatings.

In Section 4, finite element calculations are used to generate stress distribution functions along a fiber with a number of different debond lengths. These stress functions are linear summations of independent components resulting from the external load, residual stress and interfacial frictions. Fitting these functions

to the measured frequency shift distributions in the debonding phase provides details of the axial and radial stress distributions at different stages of the push-out tests, along with the debond lengths, the debond energies and the friction in the debonding phase. The friction in the sliding phase is obtained by using a shear lag model combined with the Lamé solutions for a concentric fiber and matrix

2. EXPERIMENTAL METHOD

2.1. The through-focus depth profiling method

As illustrated in Fig. 1, the fluorescence from depth z below the top surface is measured by focussing a laser beam through the fiber top surface using a microscope objective lens. By focussing to successively greater depths and measuring the frequency shift, a profile along the length of the fiber is obtained. Because of the small depth of field of the lens, the fluorescence excited will be collected from only a small volume on either side of the focal plane. The measured frequency shift $\Delta v(z)$ is hence a weighted average of that within the effective excitation volume. Therefore, the actual depth profile of the frequency shift has to be deconvoluted from that measured by using the depth of field function of the microscope. As described in Ref. [5], the depth of field function near the top surface can be measured by systematically moving the plane of focus from a position above the top surface to a position below the surface while recording the fluorescence intensity $I(z)$. The depth of field function near the top surface is then

$$g(z,0) = \frac{dI(z)}{dz}. \quad (2)$$

Here the second variable in g equals zero indicating that the depth of field function is measured at the top surface. As the distance below the top surface increases, the depth resolution deteriorates, primarily as a result of the decrease of the effective numerical aperture resulted from the ray blocking by the matrix
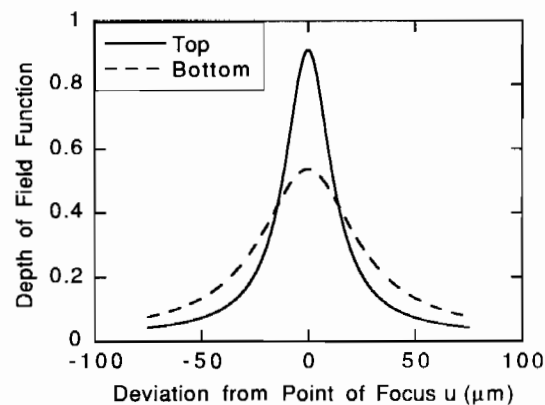

Fig. 2. The depth of field functions, measured at the top and the bottom surfaces of a sapphire fiber. The degrading of the depth resolution is caused by the ray blocking effect of the matrix, which decreases the effective numerical aperture of the system.
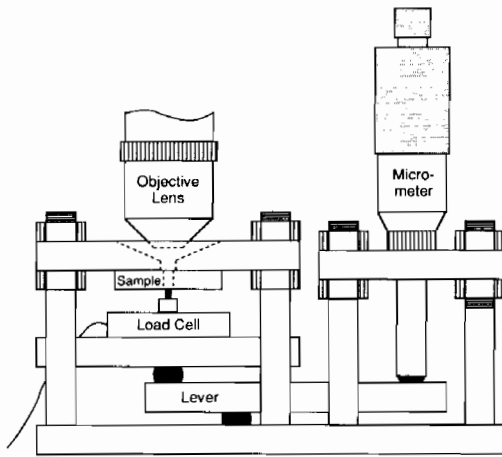
Fig. 3. The mechanical loading fixture used for the push-out test. It is designed to fit under a optical microscope for *in situ* fluorescence measurement. The dimensions are not drawn in scale. The push rod made of a Nicalon SiC fiber, for example, is only $100 \mu m$ in diameter, and the sample thickness is ~ 0.5 mm.

on the sides of the fiber. It is necessary, therefore, to obtain the depth of field function as a function of depth in order to correctly deconvolute the measured shifts at depths larger than several fiber diameters. For this purpose, the depth of field functions near the bottom surface of samples of different thicknesses were measured using the same method as described above. The depth of field function at an arbitrary depth can then be obtained by interpolation. For illustration, the depth of field function at the top surface and at $600 \mu m$ depth are plotted in Fig. 2 for our optical microscope using a 40/0.55 water immersion lens and a $50 \mu m$ collection aperture. Due to the limited number of sample thicknesses used, some error is expected in the resulting depth of field function. However, it was confirmed that for any practical purpose, any reasonable error involved in the depth of field function can only affect the deconvoluted curves within one fiber radius from the fiber bottom end, because the measured frequency shift distributions are smooth functions of depth z.

Having established the depth of field function, the measured shifts can then be related to the true shift profile $\Delta v(z)$ by

$$\overline{\Delta v(z)} = \frac{\int_{-z}^{t-z} \Delta v(z+u) g(u, z) du}{\int_{-z}^{t-z} g(u, z) du}. \qquad (3)$$

In order to evaluate the deconvolution it was assumed that the true shift $\Delta v(z)$ is a polynomial function of z but with unknown coefficients. By fitting the polynomial function convoluted with the depth of field function using equation (3) to the measured distribution, the values of the coefficients were obtained. The initially assumed function, with the coefficients obtained by fitting, is then regarded as the deconvoluted shift $\Delta v(z)$. The accuracy of this method has been previously demonstrated [5] and can

be judged later in this paper by viewing Fig. 12, where the dashed curves are the true shift Δv (the solid curves) convoluted by the depth of field function. They have excellent fit with the measured data.

2.2. Push-out method

In order to simultaneously measure both the load and the frequency shifts *in situ* during push-out tests, a special mechanical loading fixture was made to fit under the optical microscope of the microprobe. The fixture is illustrated in Fig. 3. A fiber selected for the push-out experiment was aligned with the conical opening on the top plate. The cone shape facilitates a large collection angle. The load is applied to the bottom end of the sapphire fiber by using a short push rod made of a Nicalon SiC fiber. The load is applied using a micrometer, through a lever and is measured by a load cell in series. This lever arrangement is simply for the purpose of reducing the vertical dimension of the fixture, so that it could fit under our optical microscope for the fluorescence measurements. During the push-out experiments, the load was increased incrementally. At each load step, the frequency shift profile was measured along the entire fiber by the through-focus technique described in the previous section. When the load was increased to a certain critical value, the whole fiber–matrix interface debonded and the fiber slid. The pushed-out distance was typically of the order of $10 \mu m$. The fiber was then pushed further using the micrometer so it slid for another $10 \mu m$ or so to reach a stable sliding mode. The frequency shift profile is measured again with the load applied. This profile gives information about the frictional resistance in the sliding phase.

2.3. Specimen preparation and fiber selection

Thin slices (~ 0.5 mm) of the composites, cut perpendicular to the sapphire fibers, were polished so as to obtain an optical finish at both fiber ends. The

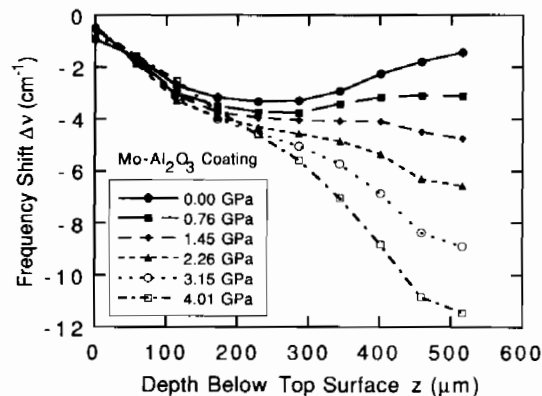Fig. 4. Measured frequency shifts Δv as a function of depth z for a fiber with Mo/Al_2O_3 coatings in the debonding phase. The top surface is at $z = 0$ and the bottom surface, where the pushing load is applied, is at $z = 516 \mu m$. Six shift depth profiles were obtained at different loads sequentially. The top curve was measured without any load, thus corresponding to the residual stresses in the fiber.

polishing facilitates the observation and the optical measurements, as well as insuring the mechanical integrity of the fiber. Because of the large statistical variations often observed in conventional push-out tests, procedures were established to select fibers for the detailed push-out studies in this work. First, visual inspections using optical microscopy were used to select fibers that were actually perpendicular to the surfaces of the composite slice. This was assessed by using the transmitted light of the microscope and comparing the relative lateral displacement between the two fiber ends. From these fibers, ones having both a circular cross-section with diameters ~ 120–130 μm, and a uniform coating were selected for the actual measurements. The depth profiling method described above was then used to measure the distribution of shifts due to residual stresses. A large fraction of the fibers measured showed irregular shift distributions, indicating inhomogeneities in the coating layers. Fibers with smooth symmetric profiles (see Figs 4 and 6) were finally selected for push-out studies.

3. FREQUENCY SHIFT DISTRIBUTIONS

Sapphire fiber (c-axis) reinforced γ-TiAl matrix composites with two different interfaces were fabricated by HIPping at UCSB for this work. One had a double coating of Mo/Al_2O_3 and the other CVD-C/Al_2O_3. The material processing methods were described elsewhere [4]. In the following, the measured shift profiles in both the debonding phase and the sliding phase are presented.

Plotted in Fig. 4 are the measured frequency shifts Δv as a function of depth z for a fiber with Mo/Al_2O_3 coatings in the debonding phase. The top surface is at $z = 0$ and the bottom surface, where the pushing load is applied, is at $z = 516 \mu$m. Six frequency shift depth profiles were obtained at successively higher applied load. The top curve was measured without any load, thus corresponding to the residual stress state in the fiber. The negative shift in the interior is consistent with there being a compressive residual stress in both the axial and radial directions developed due to thermal mismatch between the sapphire fiber and the γ-TiAl matrix (Table 1). The magnitude of the shift decreases near the top and bottom surfaces because of stress release occurring due to sample preparation. The noticeable asymmetry of the curve about the sample mid-plane is partially due to the decreasing depth resolution with increase of depth as mentioned in the last section and can be effectively corrected by deconvolution. When an increasing load, P, is applied, the magnitude of the negative shift

correspondingly increases in the lower part of the fiber, but remains essentially constant near the top end.

When the load was increased above $P = 4.01$ GPa, the whole interface debonded, and the fiber suddenly slid out by a distance of about 10μm. To reach a stable sliding mode, the fiber was pushed further so as to slide another few microns. The frequency shift profile was then measured again with the fiber under load. This profile is plotted in Fig. 5 along with two other profiles, one obtained after releasing the load and the other after the fiber had been pushed back into its initial seated position. The flat profile for the seated case indicates that the axial stress is mostly released by a slight displacement.

The behavior of the CVD-C/Al_2O_3 coated fibers is very similar to that of the Mo/Al_2O_3 coated fiber as shown in Fig. 6. However, the maximum load needed to push-out the fiber was only slightly above 2 GPa, considerably smaller than that for the Mo/Al_2O_3 coated fiber. This indicates that the CVD-C/Al_2O_3 coating has lower debond energy or has lower friction in the debonding phase. The shift profile in the sliding
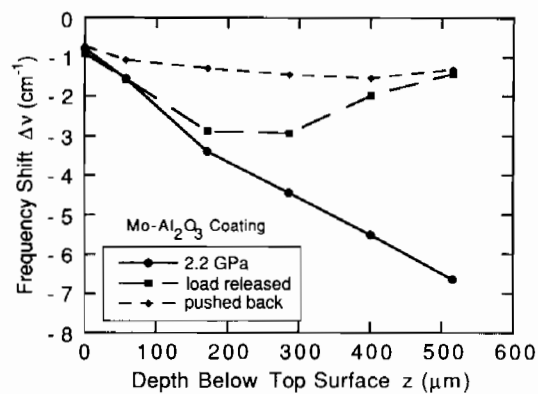

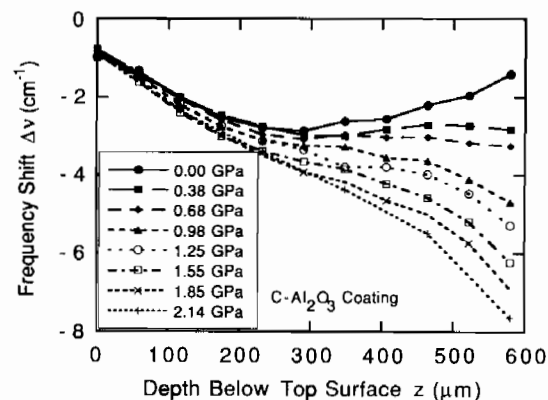Fig. 5. The shift profiles for a fiber with Mo/Al_2O_3 coatings, measured after the whole interface debonds. Three profiles correspond to cases of fiber with load applied (bullet), with load released (square) and pushed back to its seated position (diamond), respectively.

Fig. 6. Measured frequency shifts Δv as a function of depth z in the debonding phase for a fiber with CVD-C/Al_2O_3 coatings.

Table 1. Properties of fiber, matrix and coating

Property	Sapphire	γ-TiAl	Al_2O_3 coating
E (GPa)	420	173	420
v	0.27	0.33	0.27
$\alpha (10^{-6}/^\circ$C)	8.3(a), 9.0(c)	11.5	8.6

phase was also measured for the CVD-C/Al$_2$O$_3$ coating and is analyzed in the next section.

4. DATA ANALYSIS

To obtain the maximum information, such as the debond energy and interfacial friction as well as the interfacial debond length from the measured shift profiles, it is necessary to use elasticity models relating the stress distribution in the fiber to these interfacial parameters.

4.1. The debonding phase

The stress distributions in the fiber debonding phase, with the complexity introduced by the debond interface crack, cannot be accurately obtained by analytical means. We therefore employed FEM to calculate the stress distributions. The model used in the calculation is illustrated in Fig. 7. The details involved in the modeling were described in an earlier work [3]. Briefly, the axial stress σ_z and the radial stress σ_r along the core of the fiber are calculated as superpositions of several independent terms

$$\sigma_z = P f^{(1)}\left(\frac{z}{R_f}, \frac{l}{R_f}\right)$$
$$+ P_R f^{(2)}\left(\frac{z}{R_f}, \frac{l}{R_f}\right) + \tau_0 f^{(3)}\left(\frac{z}{R_f}, \frac{l}{R_f}\right) \quad (4)$$

$$\sigma_r = -N_R + P g^{(1)}\left(\frac{z}{R_f}, \frac{l}{R_f}\right)$$
$$+ P_R g^{(2)}\left(\frac{z}{R_f}, \frac{l}{R_f}\right) + \tau_0 g^{(3)}\left(\frac{z}{R_f}, \frac{l}{R_f}\right) \quad (5)$$

where P is the applied load, P_R and N_R are the axial and radial residual stresses in the fiber before the composite is sliced, τ_0 is the frictional shear stress in the debonded interface region, l is the length of the interface crack, and R_f is the fiber radius. To compare with our experiments, the stress functions f and g were calculated for a number of different debond
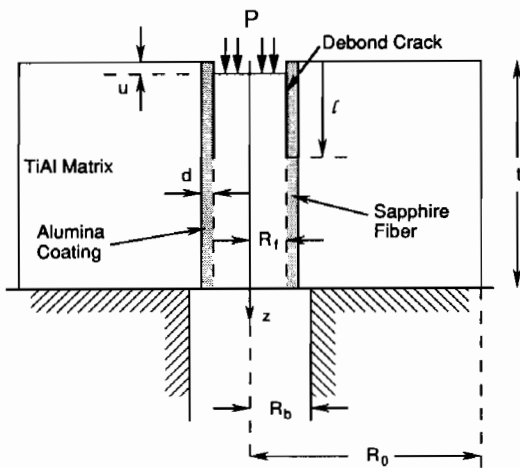

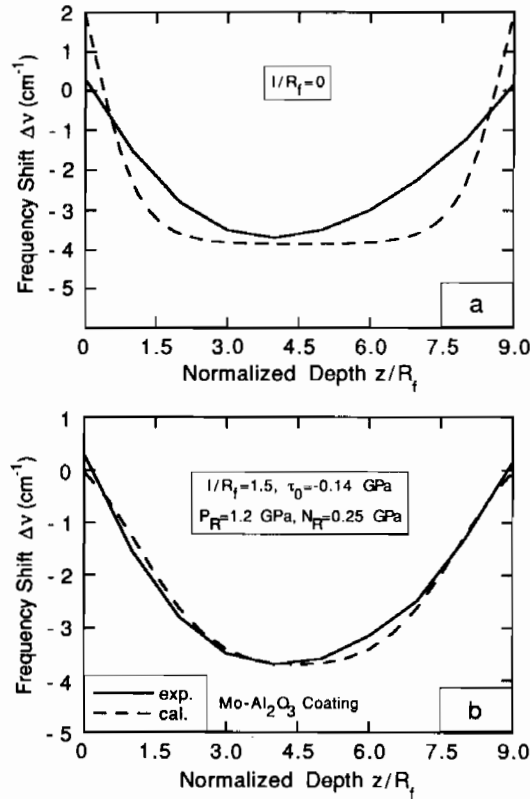Fig. 7. Schematic diagram of the push-out configuration of the finite element model.

Fig. 8. Comparison between the measured shift profile (deconvoluted) and that calculated. (a) Assuming no debond near the fiber ends; (b) assuming appropriate debond and friction near the fiber ends to match the data.

lengths, l and for the aspect ratios t/R_f corresponding to the samples used. The model used in this calculation was modified from the previous one [3] in order to incorporate the relatively thick ($\sim 10 \, \mu$m) Al$_2$O$_3$ coating on the fiber. Actual mechanical properties of the fiber, matrix and coating (listed in Table 1) were used in the finite element calculations.

In the analysis following, we first compare the measured shift profile for the residual stress with that computed so as to obtain the residual stresses P_R and N_R in the fiber before slicing. In doing so, we first assume the whole interface is completely bonded. Figure 8(a) shows the comparison between the measured shift profile (after deconvolution) and that calculated (the dashed line). The slower variations at the two ends in the measured profile suggest that in reality the interface is debonded to some extent at the two ends as a result of the sample slicing. FEM calculations of the interface shear stress, assuming no debonding, gives values near the two ends considerably higher than the interface shear strength for weak interface systems [5]. However, as illustrated in Fig. 8(b), by allowing the interface to debond about 1.5R_f from the two surfaces, the fitting between the computation and the data becomes excellent. This fitting also provides values for the axial and radial residual stress in an infinite body, P_R and N_R, respectively
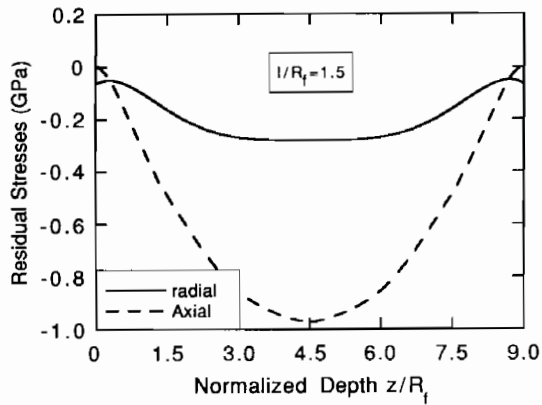
Fig. 9. Axial and radial residual stress distributions in the Mo-coated fiber after slicing.

[Fig. 8(b)]. To obtain a good correspondence, an appropriate friction stress has to be applied along the debonded section of the interface as indicated in Fig. 8(b). The negative sign indicates that the friction is preventing the fiber from moving outwards as expected. From the above fitting the detailed axial and radial residual stress distributions in the fiber in the slice are obtained as shown in Fig. 9. To assess the confidence of the above fitting, especially the values for P_R and N_R, it is instructive to compare them with elastic solutions. Since the modulus of the γ-TiAl matrix is much smaller than that of sapphire, Poisson's effects can be neglected and the following relations for the radial and axial stresses are obtained

$$N_R = E_f(\alpha_m - \alpha_a)\Delta T \frac{1}{1 + E_m/E_f} \tag{6}$$

$$P_R = E_f(\alpha_m - \alpha_c)\Delta T. \tag{7}$$

Using the materials parameters listed in Table 1, the effective temperature difference calculated using the P_R and N_R values from the fitting are $\Delta T_P = 1140°C$ and $\Delta T_N = 640°C$. Both of these values are smaller than the actual processing temperature drop, an indication of stress relaxation during cooling. The difference in effective temperature is attributed to the stress relaxation in the axial direction being less effective than in the radial direction. This is due to the fact that the fiber can not slide over long distances, so that the effective temperature difference calculated from the axial stress is much closer to the actual temperature drop of 1275°C.

Having obtained the residual stresses P_R and N_R, comparisons are made for the other profiles obtained at various loadings as illustrated in Fig. 10. The fitting is obtained by varying both the debond length and the interfacial friction in equations (4) and (5) until the best fit to the frequency shift profile is achieved. Since in the finite element calculations, the debond was only allowed to propagate up from point of loading, i.e. in the bottom part of the fiber, the lack of fitting near the top end is of little significance. Also, because the experimental data has large error within

a distance R_f from the bottom surface due to optical effects, fitting in that region is only lightly weighted.

For a load $P = 0.76$ GPa, the applied stress is still less than the axial residual stress P_R, so the monotonic loading condition assumed in the calculation is not strictly valid. As a result, the parameters from the fitting are considered less reliable. When $P = 1.45$ GPa, which exceeds P_R, it is expected that the direction of friction in the interface has been fully reversed. However, because the load is mostly balanced by P_R, relatively a small amount of friction is required to establish the equilibrium. Further, the
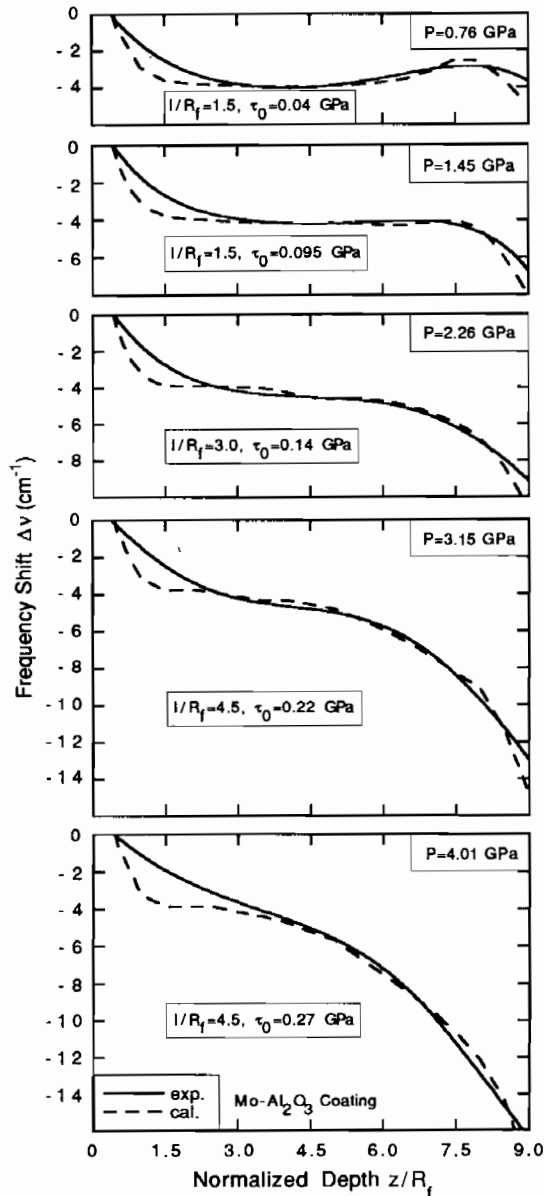

Fig. 10. Comparison of the shift profiles obtained at various loadings for the Mo/Al$_2$O$_3$ coated fiber, together with the parameters used to obtain the best fit. Since in the FEM calculations, the debond was only allowed at the bottom of the slice, the fitting near the top end carries little significance.

Table 2. Fitting parameters obtained for the Mo/Al_2O_3 coated fiber

Applied load P (GPa)	Frictional stress τ_0 (GPa)	Debond length l/R_f	Effective load P_{eff} (GPa)
0.00	−0.15	1.5	
0.76	0.04	1.5	
1.45	0.095	1.5	−0.035
2.26	0.14	3.0	0.22
3.15	0.22	4.5	−0.03
4.01	0.27	4.5	0.38

effective load exerted on the debond crack tip is also small, so that the debond length remains unchanged from the residual stress case. When the applied load is further increased, the effective load on the debond

Fig. 11. Comparison of the shift profiles obtained at various loadings for the CVD-C/Al_2O_3 coated fiber.

front also increases, which induces debond crack growth as the fitting demonstrates. The friction also increases with load for reasons which will be discussed later in Section 5.

The parameters obtained by matching the finite element calculation to the measured frequency shift are listed in Table 2 for the Mo/Al_2O_3 coating. The shift profiles measured for the CVD-C/Al_2O_3 coated fiber were analyzed similarly. The comparison between measured and calculated profiles are plotted in Fig. 11 and fitted parameters are listed in Table 3.

The debond energy can also be obtained from the data. Recognizing that the effective load applied on the debond crack, P_{eff}, is the externally applied load P balanced by the residual axial stress P_R and the frictional stress τ_0 applied through the interface shear lag

$$P_{eff} = P - P_R - \frac{2l}{R_f} \tau_0. \tag{8}$$

Dimensional analysis indicates that the elastic energy involved can be expressed in terms of the effective applied load and the debond length, l, as

$$U = \beta \frac{P_{eff}^2}{2E_f} \pi R_f^2 l. \tag{9}$$

The strain energy release rate, G, is therefore

$$G = \frac{\partial U}{\partial A} = \frac{\partial U}{\partial (2\pi R_f l)} = \beta \frac{R_f}{4E_f} P_{eff}^2. \tag{10}$$

The debond energy, Γ, can then be obtained by equating to the strain energy release rate, namely

$$\Gamma = G = \frac{\beta R_f}{4E_f} \left(P - P_R - \frac{2l}{R_f} \tau_0 \right)^2. \tag{11}$$

Using Lamé solution [3, 7], it can be shown that β is a function of the elastic properties of the fiber and the matrix and is always very close to unity. Using the average values for the effective load P_{eff}, from the data in Tables 2 and 3, values for the debond energy for the two coating systems are obtained

$$\Gamma_{Mo} = 0.57 \text{ J/m}^2$$

$$\Gamma_C = 0.03 \text{ J/m}^2.$$

Note that data obtained at relatively small loads were not used for the energy calculations, because they do not correspond to the critical loading conditions. It is worth pointing out that the apparently small value
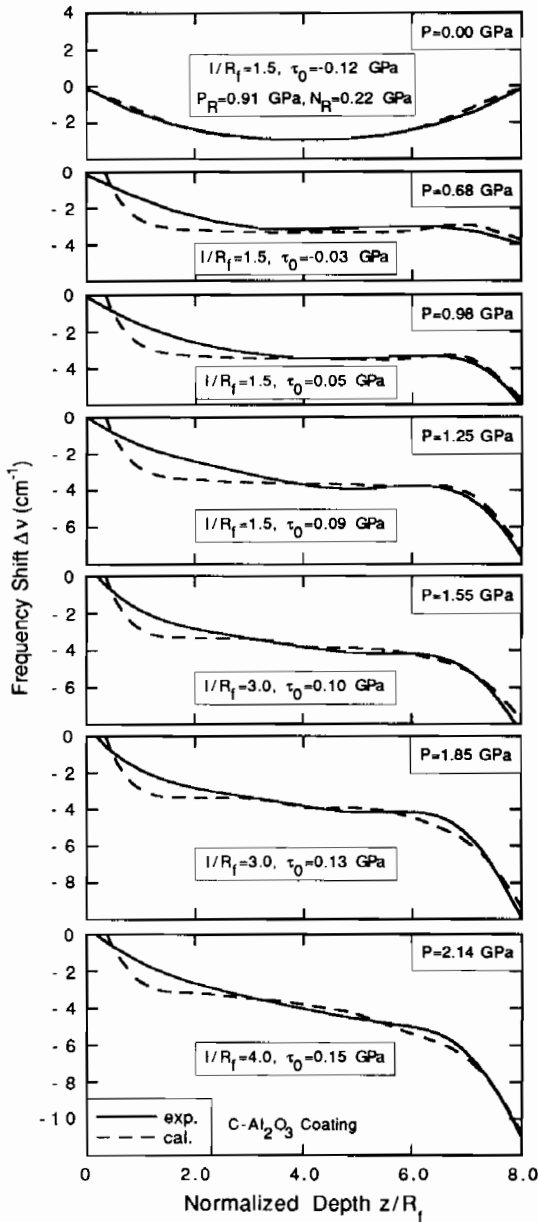
Table 3. Fitting parameters obtained for the CVD-C/Al_2O_3 coated fiber

Applied load P (GPa)	Friction stress τ_0 (GPa)	Debond length l/R_f	Effective load P_{eff} (GPa)
0.00	−0.12	1.5	
0.68	−0.03	1.5	
0.98	0.05	1.5	
1.25	0.09	1.5	0.03
1.55	0.10	3.0	−0.01
1.85	0.13	3.0	0.12
2.14	0.15	4.0	−0.01

of debond energy for the graphite coating system is not unexpected. This is because graphite has particularly low surface energy (~ 0.07 J/m^2) [8], and hence a low fracture energy. In addition, it is observed that the debond always occurs at the graphite/sapphire interface, indicating even weaker bonding at the interface. It is also noted that other workers have reported similar values [4].

4.2. The sliding phase

The frequency shift profiles in the sliding phase for the molybdenum and graphite coated fibers are plotted in Fig. 12. The solid dots are the measured shifts at the depths indicated, and the solid curve is the deconvoluted shift profile, obtained using the depth of field function, representing the true frequency shift profile. For comparison, the dashed curve is the true shift convoluted with the depth of field function, which fits the measured data, demonstrating the accuracy of the deconvolution procedure. For both fibers, the profiles are essentially linear in the center section, and show rather complicated end effects within the distance about one fiber diameter from the two surfaces. To avoid the end effects, only the center section of the curves is used to determine the value of
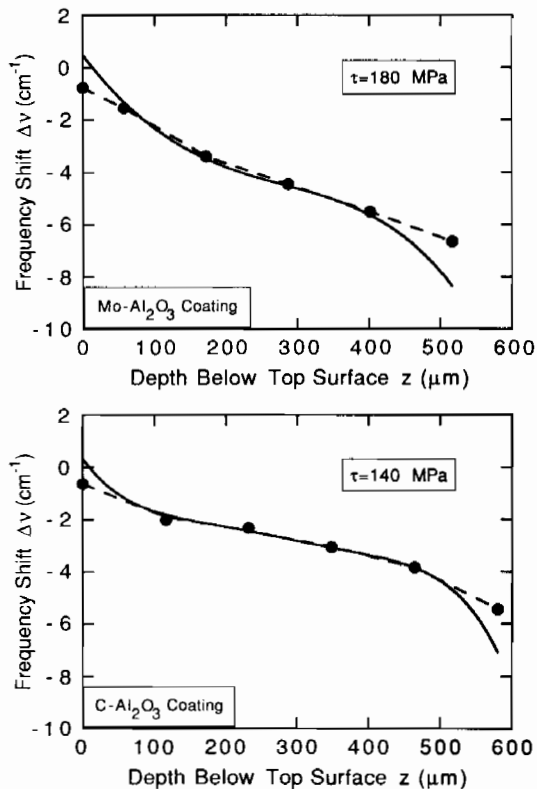

Fig. 12. Shift profiles obtained in the sliding phase for the Mo/Al$_2$O$_3$ and CVD-C/Al$_2$O$_3$ coated fiber, respectively. The solid dots are the measured shifts and the solid curve is the deconvoluted shift profile obtained using the depth of field function and therefore representing the true shift profile. The dashed curve is the true shift convoluted with the depth of field function.

the friction during sliding. This can be easily accomplished using the standard shear lag relationship

$$\frac{d\sigma_z}{dz} = -\frac{2}{R_f}\tau \quad (12)$$

together with the Lamé solution [3]

$$\sigma_r + N_R = B(\sigma_z + P_R) \quad (13)$$

where B describes the effective Poisson's effect

$$B = \frac{v_f E}{(1 - v_f)E + (1 + v)E_f} \quad (14)$$

and E and v are the Young's modulus and Poisson's ratio of the matrix.

Combining equations (1) and (13), we obtain an explicit relationship between the frequency shift and the axial stress in the sliding phase

$$\sigma_z = \frac{\Delta v + 2\Pi_a(N_R - BP_R)}{2\Pi_a B - \Pi_c}. \quad (15)$$

As in a typical push-out test, it is difficult to obtain the variation of friction along the fiber due to the variation of normal stress across the interfaces. This is because the Poisson's effect is not large enough to produce a clear curvature. Therefore the solution for the stress distributions reduces to one with an effective constant friction τ_0 [3]. Using equation (15) to fit the center section of the curves in Fig. 12, the sliding frictional stress for the two different coatings are found to be

$$\tau_{0\,Mo} = 180 \text{ MPa}$$

$$\tau_{0\,C} = 140 \text{ MPa}.$$

5. DISCUSSION

By comparing the measured frequency shift profiles with those calculated using a finite element model, we have obtained values for the debond energies, the frictional stresses and the debond length at different applied loads. In this section, we discuss their accuracies and implications.

From Tables 2 and 3, it is evident that the debond length increases as the push load increases once the load exceeds the residual axial stress P_R. This provides direct evidence that the debond growth process is a steady state crack growth process when the debond length is smaller than, or comparable to, half the fiber length. The whole interface debonds suddenly when the load is further increased. This suggests that there might be a unstable crack growth process near the top end of the fiber. Both of these observations are consistent with the theoretical predictions using FEM [3]. The debond lengths in Tables 2 and 3 appear to be multiples of the fiber radius. However, this is a consequence of the stress functions being calculated for only a limited number of debond lengths. Therefore, the actual debond length at a certain load could be either slightly larger or smaller than that obtained from the fitting. This can be

determined by examining the effective load P_{eff} at each applied load. When the applied load is larger than P_R, the effective load has to be positive, and according to equation (9), they should have the same value during steady state debond growth, for that the debond energy is always the same for a certain system. However, from Tables 2 and 3, we have both positive and negative values for the effective load, indicating that the debond lengths are indeed deviated from the true values. Since excellent fittings were obtained in the last section, it is reasonable to assume that the deviations are relatively small, and therefore the average value for the effective loading for the two coatings are relatively accurate. Consequently, the debond energies we obtained are considered relatively accurate. We can then compare the effective load at each applied load with the average effective load $\overline{P_{eff}}$ to determine whether the listed debond length is too large or too small. For example, for the Mo coating, $P_{eff} < \overline{P_{eff}}$ at $P = 1.45$ GPa, indicating that the real debond length is slightly smaller than $1.5R_f$. At $P = 2.26$ GPa, $P_{eff} > \overline{P_{eff}}$, indicating that the real debond length is slightly larger than $3.3R_f$, and so on. Using this procedure, we can qualitatively correct the uncertainty in the debond length. This data is shown superimposed with the frequency shift data in Fig. 13 illustrating the debond growth in the two systems.
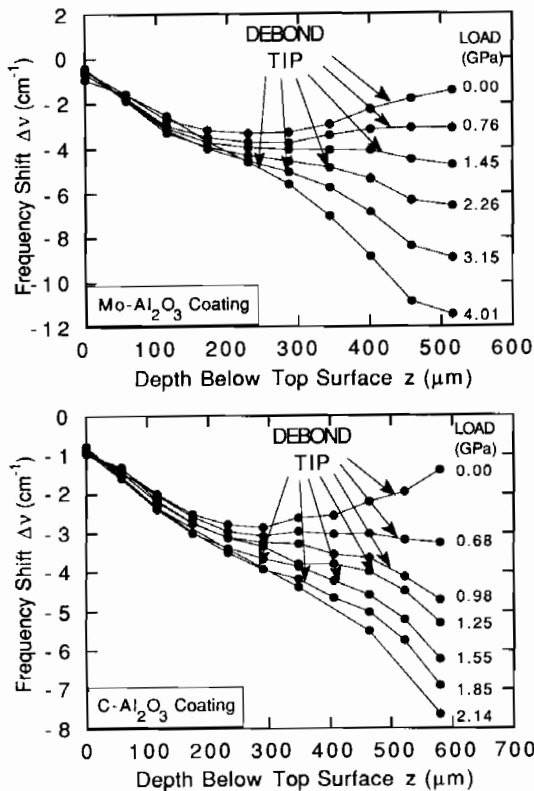

Fig. 13. Estimated positions of the tip of the debond crack as the applied load increases for the Mo/Al$_2$O$_3$ coating and CVD-C/Al$_2$O$_3$ coating, respectively.
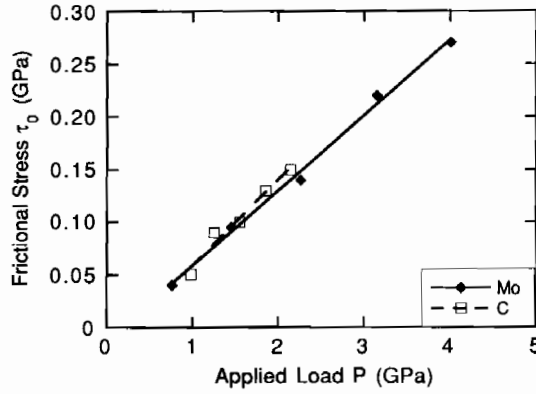

Fig. 14. The dependence of frictional stress on the applied load for the two coating systems.

One of the principal results of this work is determining frictional stress values in the debonding phase and its dependence on the type of coating. In Fig. 14 are plotted the friction–load dependence for the two coating systems. Two characteristics are evident. First, the friction increases with load. Although the friction in the calculation is assumed, for simplicity, to be constant along the interface, the load dependence clearly suggest that the friction depends on the normal stress across the interface, and may therefore be partially Coulombic. To obtain the friction law, the normal stress averaged across the length of the debonded interface was calculated for each applied load. The frictional stress as a function of such normal stress is then plotted in Fig. 15 for the two coating systems. Instead of obeying a linear, Coulombic dependence, the relationship appears to be parabolic, suggesting that the friction may depend on small displacements of the fiber from its seated position. Such asperity effects have been reported previously [4, 9] and are addressed elsewhere [10, 11]. The second characteristic feature is that the frictional stress for the two different coating systems is quite similar. This strongly suggests that the friction in the debonding phase depends primarily on the interface morphology, which in turn is determined by the
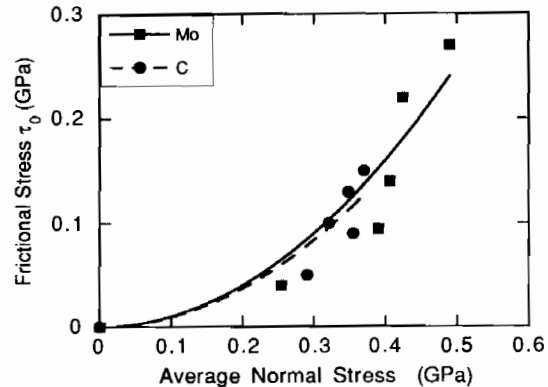

Fig. 15. The dependence of frictional stress on the average normal stress across the debonded interface for the two coating systems. The curves show parabolic fittings.

sapphire fiber surface morphology, rather than on the coating material *per se*. Therefore, in order to reduce the friction in the debonding phase, it is important to improve the fiber surface smoothness. Further, the large difference in the maximum load needed to push-out the fibers and in the debond energy suggests that the debond energy determines the push-out load, and therefore plays an important role in determining the composite property.

Finally, we have also been able to determine the friction in the sliding phase for the two systems. The values obtained here and in other studies using conventional push-out techniques agree rather well [4], with the friction for the CVD-graphite coating usually exhibiting smaller values than that of the Mo coating. We can therefore conclude that in the sliding phase, the properties of the coating material are also important for frictional sliding.

6. CONCLUSION

By measuring *in situ* the stress distributions along sapphire fibers at different stages of the push-out test, and comparing them with those calculated using a finite element model, the key mechanical parameters controlling the push-out process have been determined, and their implications discussed.

The measurements of the residual stress distributions along the fibers before loading and comparison to the computations provide the values of the residual stresses in the composite prior to slicing a thin section for the push-out test. They also give the extent of interface debonding caused by the slicing.

It is observed that the debond length increases stably with increasing applied load when the debond is not significantly greater than half of the fiber length. This provides clear evidence that the debonding process in this region is a steady state crack growth process. The sudden debond of the interface afterwards suggests that there is also an unstable crack propagation process near the end. These observations agree with the predictions made using earlier FEM calculations [3].

The interfacial friction in the debonding phase is shown to increase with the applied load. Further, the dependence of the friction on the average normal stress across the debonded interface is nearly parabolic. These observations suggest that the fric-

tion is partially Coulombic and is strongly influenced by the asperities along the interface. In the debonding phase, the displacement is very small, so that the fiber is in an unseating process, and hence the effective friction may depend on the displacement, in addition to the normal stress. Another significant feature of the friction in the debonding phase is that it is very similar for the two coating systems. This further suggests that the interface morphology largely determines the interface friction, while the coating material plays a less important role. However, the friction in the sliding phase obtained for the two coating systems are different in value and are very similar to those obtained by conventional push-out tests [4].

The debond energies were also obtained for the two interfaces. For the CVD-C coated fiber, the energy is about one order of magnitude smaller than that for the Mo coated fiber, which explains why the load required to push-out a CVD-C coated fiber is only half of that for the Mo coated one. The implication of this is that the debond energy will also significantly influence the fracture properties of composites.

REFERENCES

1. D. B. Marshall, *J. Am. Ceram. Soc.* **67**, C259 (1984).
2. P. D. Warren, T. J. Mackin and A. G. Evans, *Acta metall. mater.* **40**, 1243 (1992).
3. L. C. Liang and J. W. Hutchinson, *Mech. Mater.* **14**, 207 (1993).
4. T. J. Mackin, J. Y. Yang, C. G. Levi and A. G. Evens, *Mater. Sci. Engng A* **161**, 285 (1993).
5. Q. Ma and D. R. Clarke, *Acta metall. mater.* **41**, 1817 (1993).
6. R. G. Munro, G. J. Piermarini, S. Block and W. B. Holzapfel, *J. appl. Phys.* **57**, 165 (1985).
7. J. W. Hutchinson and H. M. Jensen, *Mech. Mater.* **9**, 139 (1990).
8. R. J. Good, L. A. Girifalco and G. Kraus, *J. Phys. Chem.* **62**, 1418 (1958).
9. T. J. Mackin, P. D. Warren and A. G. Evans, *Acta metall. mater.* **40**, 1251 (1992).
10. W. C. Carter, E. P. Butler and E. R. Fuller Jr, *Scripta metall. mater.* **25**, 579 (1991).
11. L. C. Liang and J. W. Hutchinson, in preparation.